PNAS RESEARCH ARTICLE | PHYSICS

The geometry of jamming algorithms in the random Lorentz gas

Giampaolo Folena[a,1], Patrick Charbonneau[b,c,1], Peter K. Morse[d], Rafael Díaz Hernández Rojas[e], and Federico Ricci-Tersenghi[f]

Edited by Srikanth Sastry, Jawaharlal Nehru Centre for Advanced Scientific Research, Bangalore, India; received October 25, 2024; accepted September 18, 2025 by Editorial Board Member Daan Frenkel

Deterministic optimization algorithms unequivocally partition a complex energy landscape into inherent structures (ISs) and their respective basins of attraction. Can these basins be defined solely through geometric principles? This question is paramount to understanding hard sphere jamming, a key model of disordered matter. We here address the issue by proposing a geometric class of gradient descent–like algorithms, which we use to study a system in the hard-sphere universality class, the random Lorentz gas. The statistics of the resulting ISs is found to be strictly inherited from those of Poisson–Voronoi tessellations. The landscape roughness is further found to give rise to a hierarchical organization of ISs, which various algorithms explore differently. In particular, greedy and reluctant schemes tend to favor ISs of markedly different densities. The resulting ISs nevertheless robustly exhibit a universal force distribution, thus confirming the geometric nature of the jamming universality class. Along the way, the physical origin of a dynamical Gardner transition is identified.

jamming universality | jamming algorithms | nonsmooth optimization | stochastic geometry | Gardner transition

Jamming granular systems—either for sand play or industrial transport (1)—ubiquitously gives rise to disordered materials; so does supercooling many liquids. Over a quarter of a century ago, this analogy led Liu and Nagel to propose a unification of the two processes under a single conceptual umbrella (2). Their jamming phase diagram has since inspired fields as diverse as robotics (3), tissue mechanics (4), and neural networks (5, 6). It has also seeded a substantial research effort aiming to flesh out the original proposal itself (7–9).

In this last respect, particularly significant strides have been made from the study of simple liquids in the limit of infinite spatial dimensions, $d \to \infty$ (10). This seemingly abstract construction has indeed rationalized jamming marginality and its associated isostaticity (11–13), and made stunningly accurate predictions about the nontrivial scaling of the distribution of weak interparticle forces $P_F(f) \sim f^\theta$ and small interparticle gaps $P_H(h) \sim h^{-\gamma}$ down to $d = 2$ (12, 14–19). Despite jamming being an inherently out-of-equilibrium and hence a protocol-dependent phenomenon, its criticality is seemingly universal. That robustness, however, remains largely unexplained.

Another—in some ways more salient—theoretical challenge entails predicting the jamming density. For three-dimensional hard spheres, that quantity had long been understood to be algorithm invariant, with a volume fraction of about 64%, thus cementing random close packing (RCP) as a physically robust and universal concept. Over the last couple of decades, however, the confounding role played by various factors, such as the degree of crystallinity (20) and the preparation scheme (17, 21), including details of the initial conditions (17, 22), have softened confidence in the robustness of RCP. At this point, even identifying a physically [let alone mathematically (23, p. 240–2)] meaningful substitute remains an open challenge. In light of this, several alternatives have been offered as replacements for RCP: numerical extensions of the equilibrium liquid line (24), the endpoint of absorbing-state processes (25), the most random jammed configuration (20), and the densest isostatic packing (26). However, using these definitions to estimate a density of interest in practice often means introducing some degree of algorithmic arbitrariness such as explicit or implicit thermalization (21).

Some of us have recently proposed that "the lowest jammed density achievable through bulk physical processes involving monotonic compression," $\varphi_{\mathrm{J}0}$, might be a well-defined quantity (21). Put differently, to determine $\varphi_{\mathrm{J}0}$ one needs to identify an algorithm for jamming hard spheres akin to gradient descent (GD) for energy minimization in that it is both greedy and local.

This idea is not new. In the mid-1980s, Stillinger and Weber systematically approximated the jammed inherent structures (ISs) of hard spheres by using GD for systems with ever steeper interactions (27). More recently, Torquato and Jiao have formulated a linear programming scheme for hard spheres to reach jamming (28)—later

Significance

Crunching hard grains together leads to their rigidification, irrespective of how the system is prepared. While certain features of the resulting jammed materials—e.g. their contact force distribution—are remarkably invariant, others—e.g. their density—can vary quite a bit. The underlying physics at play behind either, however, remains unclear. Such a purely geometric system begs for an explanation of the same nature. This work addresses the problem by employing a minimal stochastic-geometric model and by identifying a class of jamming schemes that explore its hierarchically complex landscape. This perspective on jamming further offers insights into the broader class of optimization problems under hard constraints.

Author affiliations: [a]Dipartimento di Fisica, Sapienza Università di Roma, Roma 00185, Italy; [b]Department of Chemistry, Duke University, Durham, NC 27708; [c]Department of Physics, Duke University, Durham, NC 27708; [d]Department of Physics, Seton Hall University, South Orange, NJ 07079; [e]Institut für Theoretische Physik, Georg-August-Universität Göttingen, Göttingen 37077, Germany; and [f]Dipartimento di Fisica, Sapienza Università di Roma, Istituto Nazionale di Fisica Nucleare–Sezione di Roma1, Consiglio Nazionale delle Ricerche Istituto di Nanotecnologia, Roma 00185, Italy

---

Author contributions: G.F. and P.C. designed research; G.F., P.K.M., and R.D.H.R. performed research; G.F. and P.C. analyzed data; and G.F., P.C., P.K.M., R.D.H.R., and F.R.-T. wrote the paper.

The authors declare no competing interest.

This article is a PNAS Direct Submission. S.S. is a guest editor invited by the Editorial Board.

[1] To whom correspondence may be addressed. Email: giampaolofolena@gmail.com or patrick.charbonneau@duke.edu.

This article contains supporting information online at https://www.pnas.org/lookup/suppl/doi:10.1073/pnas.2422096122/-/DCSupplemental.

generalized as CALiPPSO (29, 30)—and Lerner et al. have formulated an overdamped compression scheme for that same purpose (12). For various reasons, however, the effectiveness of these schemes at attaining φ_{J0} has not been systematically evaluated. (See ref. 21 for an effort along this direction.) More problematically, a qualitative understanding of the similarities and differences between these schemes has yet to be teased out. Even in the simplifying limit of $d \to \infty$ (out-of-equilibrium) insights are in short supply (31).

In order to shed light on both jamming robustness and density, we here consider the random Lorentz gas (RLG), a single-particle model that belongs to the hard sphere universality class in the limit $d \to \infty$ (32). But what is jamming—an ostensibly collective phenomenon—in a single-particle system? Inspired by a recent geometrical study (33) and connections between the Voronoi network and jamming (34), we identify jammed ISs as inscribed spheres and propose a class of GD-like volume ascent (VA) algorithms for identifying them. This approach determines φ_{J0} for the RLG and illuminates the algorithm dependence of jamming more generally. Remarkably, we also find that $P_F(f)$ converges to the anomalous infinite-dimensional hard-sphere scaling for all algorithms, thus illuminating its geometrical origin. These advances not only pave the way for a deeper understanding of jamming but also hold the potential for improving high-dimensional optimization with hard constraints, which notably appear in the fields of computational geometry (35–37) and robust optimization (38).

The Entropic Landscape of the RLG. Recall that the RLG consists of one spherical tracer evolving in the space unoccupied by N hard (yet noninteracting) fixed spherical obstacles within a box of volume V. These obstacles, which are distributed uniformly at random, form a Poisson process with number density (or intensity) $\rho = N/V$. One RLG convention assigns both tracer and obstacles the same sphere radius $r/2$; equivalently, one could consider a point tracer and obstacles of radius r, or point obstacles and a tracer of radius r. To ease visualization, we here mainly follow this last convention. To make densities unitless and of order one in all d, we further set $\rho = 1$ and define the reduced volume fraction $\hat{\varphi} = \rho V_d r^d/d = V_d r^d/d$ with V_d the volume of a d-dimensional unit sphere (32).

To identify the ISs of the RLG, we follow the approach developed for random polytopes in ref. 33. At equilibrium, r is constant; compression inflates r. At each tracer position $\mathbf{x}$ there exists a maximal sphere (sph) of radius r_{sph} that does not overlap with any obstacles. An IS is obtained when that radius r_{sph} can no longer locally grow by changing position $\mathbf{x}$, without creating overlaps with obstacles, hence determining r_{IS}. The resulting tracer position, $\mathbf{x}_{\mathrm{IS}}$, is then equidistant from $d+1$ obstacles: Fewer would not ensure mechanical stability, and more—given the Poissonian nature of the obstacles—would be highly improbable. Per the Maxwell criterion, the resulting IS is therefore isostatic. From this analysis, an unambiguous determination of all IS for a given obstacle distribution follows (Fig. 1*A*). In geometrical terms, each point equidistant to $d+1$ obstacles is a Voronoi vertex (VV) or, equivalently, a circumcenter of the dual Delaunay tessellation. As shown in ref. 39, a VV is stable if it is contained within the respective Delaunay simplex (DS), and unstable if not. Only the former are ISs (Fig. 1 *A*–*D*).

Number of ISs. Having established that each IS is the circumcenter of a stable DS, we now obtain a count of these features (per unit volume), $\mathcal{N}_{\mathrm{IS}}$, as a function of their packing fraction at jamming, $\hat{\varphi}_{\mathrm{IS}}$ (or, equivalently, r_{IS}). This analysis therefore provides a measure of configurational entropy of ISs, $\Sigma_{\mathrm{IS}} = \ln \mathcal{N}_{\mathrm{IS}}$.

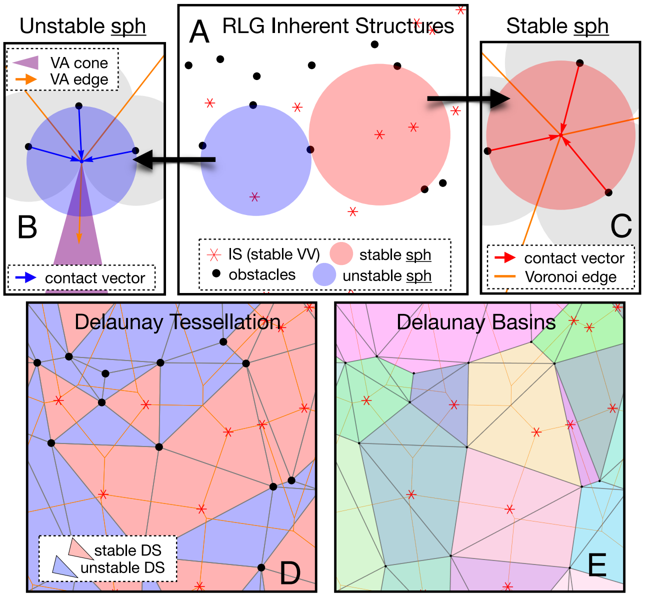

Fig. 1. (*A*): Geometric (or entropic) landscape of the $d = 2$ RLG with obstacles (black dots) and ISs (red stars). A sph is in contact with $d + 1$ obstacles. It is unstable if these contacts are cohemispheric (light blue) and stable otherwise (light red). Contact vectors for the (*B*) unstable and (*C*) stable sph in (*B*), along with the VA cone of possible expansion directions (purple) for the former. (*D*): Delaunay tessellation of the sample in (*A*). An unstable DS does not contain its circumcenter (blue), while a stable DS does (red), thus identifying an IS (stars). (*E*): Delaunay basins from Eq. **4** (different colors) of the sample in (*A*). These basins are generally composed of one stable DS and zero or more surrounding unstable DS. The DSs (black lines) and the Voronoi tessellation (orange lines) are provided as reference.

A result from stochastic geometry (40), which holds for unbounded systems, gives that the density of DS—both stable and unstable—of a given $\hat{\varphi}$ per unit volume $\mathcal{N}_{\mathrm{DS}}(\hat{\varphi})$ is proportional to the Gamma probability distribution function $p_\Gamma(\hat{\varphi}) = d^d e^{-d\hat{\varphi}} \hat{\varphi}^{d-1}/\Gamma(d)$, i.e.,

$$\mathcal{N}_{\mathrm{DS}}(\hat{\varphi}) = N_{\mathrm{DS}}(d) p_\Gamma(\hat{\varphi}), \qquad [1]$$

where $N_{\mathrm{DS}}(d)$ is the average number of DSs per unit volume.[*] Remarkably, given (41, Thm. 10.4.4), the geometry of each DS is statistically independent of its radial size—or, equivalently, the stability condition is statistically independent from the radial size of the cell—and hence

$$\frac{\mathcal{N}_{\mathrm{IS}}(\hat{\varphi})}{N_{\mathrm{IS}}(d)} = \frac{\mathcal{N}_{\mathrm{DS}}(\hat{\varphi})}{N_{\mathrm{DS}}(d)} = p_\Gamma(\hat{\varphi})\ . \qquad [2]$$

The number of ISs per unit volume $N_{\mathrm{IS}}(d) = \mathcal{V}_{\mathrm{IS}}(d) N_{\mathrm{DS}}(d)$, however, is strongly reduced by a proportionality factor that can be decomposed as $\mathcal{V}_{\mathrm{IS}}(d) = \mathcal{P}_{\mathrm{IS}}(d)\mathbb{E}[v_{\mathrm{IS}}]/\mathbb{E}[v_{\mathrm{DS}}]$, where $\mathcal{P}_{\mathrm{IS}}(d)$ is the fraction of stable DSs and $\mathbb{E}[v_{\mathrm{IS}}]/\mathbb{E}[v_{\mathrm{DS}}]$ is the ratio of the expected volume of stable DSs to the expected volume of all DSs.

Fig. 2 shows that numerical results obtained using the standard qhull library (42) for Voronoi tessellation agree with Eqs. **1** and **2**, as expected. Because $\int d\hat{\varphi}\ \hat{\varphi} p_\Gamma(\hat{\varphi}) = 1$ for all d, we then have that sampling ISs uniformly at random gives $\mathbb{E}_{\mathrm{IS}}[\hat{\varphi}] = 1$ for all d. Numerics further reveal that $\mathcal{P}_{\mathrm{IS}}(d)$ is exponentially suppressed

---

[*] Low-d results are known (40): $N_{\mathrm{DS}}(d = 2) = 2$, $N_{\mathrm{DS}}(3) = 6.76\ldots$, $N_{\mathrm{DS}}(4) = 31.77\ldots$.

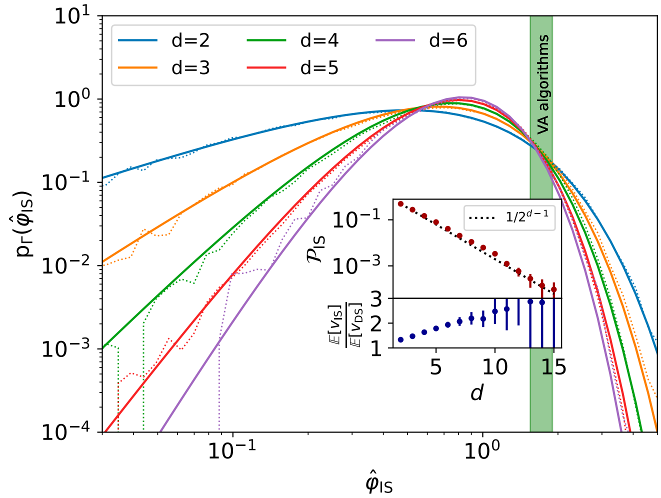

Fig. 2. Probability distribution of ISs with packing fraction $\hat{\varphi}_{\rm IS}$ in $d = 2\ldots6$. The expression in Eq. **2** (full lines) agrees with the numerical enumeration of stable ISs (dotted lines). Note that the distribution peaks at mode$[\hat{\varphi}_{\rm IS}] = (d-1)/d$ and that the expected jamming packing fraction is $\mathbb{E}[\hat{\varphi}_{\rm IS}] = 1$ for all d. VA algorithms, by contrast, typically reach significantly larger values, as shown here for $d = 2\ldots6$ (green band). (*Inset*) The proportion of stable DSs (points) empirically scales as $1/2^{d-1}$ (dotted line), while the ratio between the expected volume of stable DSs and the expected volume of all DSs grows sublinearly in d.

in d, approximately scaling as $1/2^{d-1}$,[†] while $\mathbb{E}[v_{\rm IS}]/\mathbb{E}[v_{\rm DS}]$ grows slower than exponential with d (Fig. 2, *Inset*). In other words, in high d, unstable DSs exponentially dominate both in number and in volume over stable DSs.

VA Algorithms and Geometry. Despite the scarcity of stable DSs, some algorithms can nevertheless reach them in polynomial time. To this effect, we here specifically define volume ascent (VA) schemes as the class of local algorithms which monotonically inflate $r_{\rm sph}$. Note that the VA problem can be formulated more generally within the mathematical framework of nonsmooth optimization (44, 45). Specifically, $r_{\rm sph}$ is a continuous but nondifferentiable function of $\mathbf{x}$, thus defining a rough landscape with many kinks, for which standard optimization techniques are ineffectual. Our analysis of stable DSs, therefore, provides insight into the dynamics of these algorithms more generally.

For VA schemes, first, each unstable Delaunay simplex is associated with a Voronoi vertex that presents a cone of possible VA directions (VA cone), within which the edges of the Voronoi tessellation identify a subset of specific VA pathways (VA edges). While in $d = 2$ an unstable Voronoi vertex contains only one such VA edge (Fig. 1*B*), for $d > 2$ that number varies between 1 and $d - 1$.

Second, because the volume fraction of stable DSs is exponentially suppressed with increasing d, the system volume is almost completely filled with unstable DSs in the large d limit. Any VA algorithm must therefore flow between many unstable VVs before reaching an IS. Because VVs can be hierarchically connected through VA edges, selecting a specific VA algorithm is equivalent to selecting one such compression pathway (either along VA edges or in between them).

Among all possible VA algorithms, we first consider the greediest one, VA-max. The tracer displacement, $\mathbf{dx}$, is then chosen to maximize the growth of the sph radius, $r_{\rm sph}$, at each position $\mathbf{x}$,

$$\mathbf{dx} = \underset{\tilde{\mathbf{dx}}}{\operatorname{argmax}}\; r_{\rm sph}(\mathbf{x} + \tilde{\mathbf{dx}}), \tag{3}$$

thus making it a direct analog of GD for energy minimization. (For a broader definition of steepest descent in nonsmooth landscapes, see ref. 45.) Fig. 3*A* illustrates the process for $d = 2$. Starting from a point tracer originally at $\mathbf{x} = \mathbf{x}_{\rm in} = \vec{0}$, the maximal radius available $r_{\rm sph}$ is equal to the distance to the closest obstacle $|\mathbf{p}_0|$. Following Eq. **3**, the tracer then moves radially from the closest obstacle ($\mathbf{dx} \propto -\mathbf{p}_0$) while its radius grows as $r_{\rm sph} = |\mathbf{x} - \mathbf{p}_0|$, until the tracer kisses a second obstacle at $\mathbf{p}_1$. Its center is then equidistant from $\mathbf{p}_0$ and $\mathbf{p}_1$. The subsequent dynamics follows the Voronoi hyperplane defined by points equidistant from both $\mathbf{p}_0$ and $\mathbf{p}_1$, until the sph reaches a third obstacle at $\mathbf{p}_2$. In $d = 2$, the tracer is then equidistant from $d + 1 = 3$ obstacles, and its center is on a Voronoi vertex (VV), by definition. In general d, the center of the sph reaches a VV by d Gram–Schmidt projections of the initial growth direction $-\mathbf{p}_0$ onto span$\{\mathbf{p}_1, \ldots, \mathbf{p}_d\}$, thus defining $\hat{\varphi}_{\rm VV}$.[‡]

If this VV is stable, then an IS has been reached and the dynamics stops. Otherwise, the trajectory flows in the greediest direction inside the VA cone, which necessarily lies along one of the VA edges (Fig. 1*B*). For $d = 2$, because the VA cone contains only one such edge, VA-max follows it up to the next Voronoi vertex. In $d > 2$ at each VV the greediest VA edge is followed until another VV is found, and so on (*SI Appendix*).

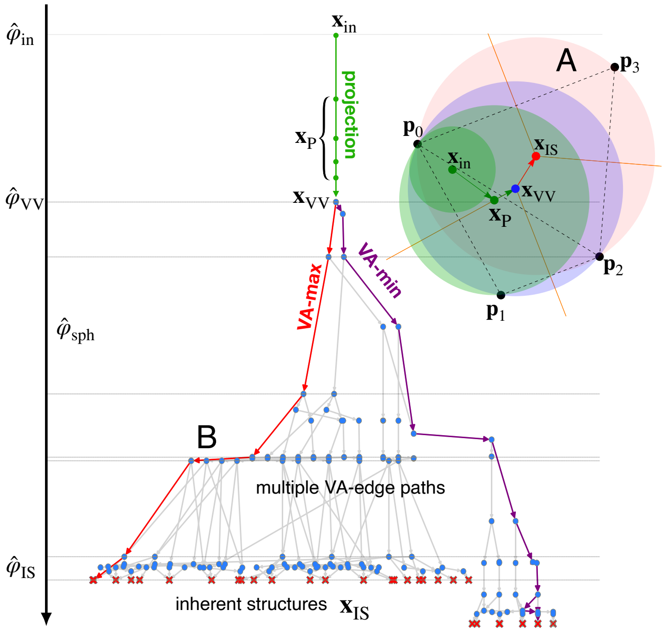

Fig. 3. (*A*): Schematic of the VA-max algorithm for the $d = 2$ RLG. The tracer starts at $\mathbf{x}_{\rm in}$, moves radially from $\mathbf{p}_0$ until it reaches the Voronoi line at $\mathbf{x}_{\rm P}$, and then follows it until reaching the first VV at $\mathbf{x}_{\rm VV}$. It subsequently follows the VA edge until $\mathbf{x}_{\rm IS}$, which corresponds to a vertex of the Voronoi tessellation. (*B*): In generic d, the VA cone at each VV can present up to $d-1$ VA edges, thus giving rise to the multipath structure of the VA-edge algorithm. After the initial d-step projection up to $\hat{\varphi}_{\rm VV}$ (green), multifurcation along various VA edges results in different ISs (red crosses). Path coalescence can also arise but is rare. The VA-max (red) and the VA-min (purple) paths are the greediest and the most reluctant VA-edge algorithms, respectively. For this $d = 5$ example, the abscissa is chosen so as to minimize path crossings.

[†] This ratio is akin to Wendel's theorem (43), which predicts that $1/2^d$ of simplexes are stable when sampling $d + 1$ vertices on a d-dimensional sphere. The two cases, however, differ because random Delaunay simplexes tend to be more stable than random simplexes.

[‡] This process is equivalent to projecting the initial point onto one of the vertexes of the Voronoi polytope defined by points that are closer to $\mathbf{x}_1$ than to any other obstacle.

Fig. 3*B* illustrates the VA-max algorithm among the graph of VA edges connecting VVs. All other paths are reluctant VA-edge schemes. Among those, we define the most reluctant VA-min, which selects the direction of least growth at each VV. (VA-min, however, is not the most reluctant algorithm of the overall VA class, for which an inf does not exist.) As expected for systems with complex landscapes (46), more reluctant algorithms typically achieve larger packing fractions $\hat{\varphi}_{\mathrm{IS}}$, over a larger number of steps than VA-max (*SI Appendix*). The graph of all possible VA-edge paths from the initial projection $\mathbf{x}_{\mathrm{VV}}$ to all final ISs also presents two key features of rough landscapes: multifurcation and coalescence. The former is directly connected to the presence of multiple VA edges at each VV and its probability grows with d; the latter is the convergence of two trajectories that have previously bifurcated and its probability vanishes as d increases.

Fractal Basins. The basin of attraction $\mathcal{B}^{\mathrm{alg}}_{\mathrm{IS}}$ for a given (deterministic) algorithm is the ensemble of all initial configurations $\mathbf{x}_{\mathrm{in}}$ that reach a same IS. Its volume is proportional to the algorithmic probability to sample that IS. For VA-max in $d = 2$, a geometrical analysis of these basins is straightforward. Because every trajectory starting within a given DS flows toward the VV at its circumcenter, the flow of trajectories clusters all DSs that flow to a same IS. The basin of attraction of each IS is therefore a pure Delaunay basin

$$\mathcal{D}_{\mathrm{IS}} = \{a \mid \mathrm{circ}(a) = \mathbf{x}_{\mathrm{IS}} \text{ or } \exists b \in \mathcal{D}_{\mathrm{IS}} \text{ s.t. } \mathrm{circ}(a) \subset b\}\,, \qquad [4]$$

where a, b are DS and circ(a) is the circumcenter of a. Put differently, the basins of attraction can be decomposed as one stable DS surrounded by unstable DSs. As can be seen in Fig. 1*E*, in $d = 2$ the resulting basins are heterogeneous in shape and, in contrast to the cells in Voronoi or Delaunay tessellations, not necessarily convex. From the definition of a Delaunay basin, a simple greedy algorithm naturally follows: At each step, the tracer moves to the circumcenter defined by the vertices of the Delaunay simplex (DS) that currently contains it. In other words, it displaces the tracer to a nearby Voronoi vertex that most increases its radius (*SI Appendix*). Remarkably, in the RLG, this procedure is equivalent to the CALiPPSO linear optimization algorithm (29, 30). As a result, basins of attraction for this scheme exactly correspond to Delaunay basins in all d. For VA-max in $d > 2$, although a similar decomposition does not exactly describe basins due to the initial simplex having more than one unstable direction, numerical results suggest it is nevertheless a very good approximation, especially for large d (*SI Appendix*).

The basin structure of any greedy algorithm naturally forms a tree-like graph. The root vertex is then the stable DS, each node corresponds to a simplex, and each edge represents the algorithmic step from one simplex to another. Fig. 4 *A* and *B* depict the tree-like organization of DSs within a Delaunay basin, derived using the Eq. **4** definition, after numerically tessellating the space into DSs. Given that the number of simplexes within a typical basin scales exponentially with d (due to the above-mentioned scarcity of stable DSs), we expect that, even in moderately high dimensions, basins exhibit intricate graph structures with nontrivial fractal dimensions (*SI Appendix*).

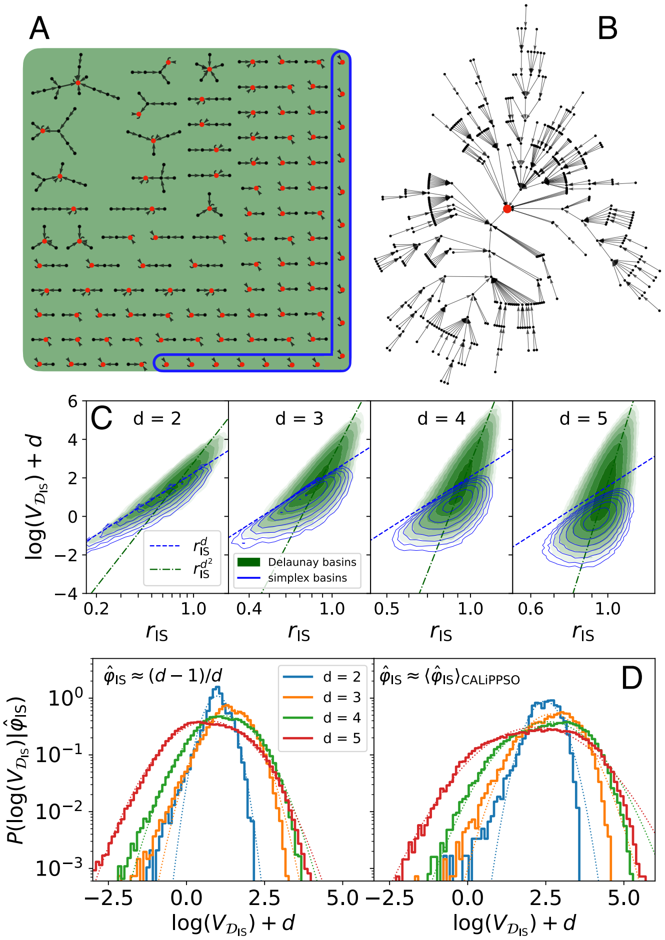

Fig. 4. (*A*): Tree graphs of the Delaunay basins in Fig. 1*E* as described in the text. The fraction of basins with a single DS (circled in blue) decreases exponentially as d increases. (*B*): Tree graph of a large Delaunay basin in $d = 4$ illustrating the growing fractal-like nature of these basins with d. (*C*): Joint distribution of the logarithm of the Delaunay basin volume $\log(V_{\mathcal{D}_{\mathrm{IS}}})$ and the circumradius r_{IS} in $d = 2 \dots 5$ from direct Delaunay tessellation (*SI Appendix*). The volume of basins composed of one simplex is upper bounded by the volume of regular simplexes (blue dashed line). The noncompact dependence of the volume of Delaunay basins (green cloud) trends consistently with $\propto r_{\mathrm{IS}}^{d^2}$ (green dashed-dotted line), hinting at their fractal-like nature. Both blue and green clouds are pdfs with contour lines at 2^k with $k = -5 \dots 1$. (*D*): Probability distribution of the logarithm of the Delaunay basin volume, conditioned on the packing fraction: the mode of the distribution, $\hat{\varphi}_{\mathrm{IS}} = (d-1)/d$, and a typical value obtained from the dynamics, $\hat{\varphi}_{\mathrm{IS}} = \langle\hat{\varphi}_{\mathrm{IS}}\rangle_{\mathrm{CALiPPSO}}$. Log-normal fits (dotted lines) are provided as reference.

To further characterize this structure, we consider the joint distribution of basin volume $V_{\mathcal{D}_{\mathrm{IS}}}$ and circumcenter radius r_{IS} (or equivalently, packing fraction) in Fig. 4*C*. In all d, the basin volume growth is consistent with $\propto r^{d^2}$, much faster than for compact objects, for which $V \propto r^d$. (Recall that the RLG is a single-particle system, and hence its phase space is d-dimensional.) Fig. 4*D* presents the log-distribution of volumes conditioned on packing fraction for $d = 2, 3, 4, 5$. Two packing fractions are considered: i) the mode of the uniform sampling distribution, and ii) the typical value reached dynamically, $\langle\hat{\varphi}_{\mathrm{IS}}\rangle_{\mathrm{CALiPPSO}}$. In both cases, the distributions flatten as dimension increases. In all dimensions, the extension of the Edwards hypothesis to single-particle systems—namely, the assumption that all configurations at fixed $\hat{\varphi}_{\mathrm{IS}}$ are sampled uniformly at jamming (47, 48)—appears to be violated. For the first packing fraction, the distribution is approximately log-normal, consistent with observations in multiparticle systems (49). However, the distribution conditioned on the second packing fraction is significantly broader, indicating that the basins sampled by VA compression are highly heterogeneous in size. Interestingly, this behavior contrasts with what was reported for systems of polydisperse disks (50, 51), for which the distribution narrows instead, consistent with the Edwards hypothesis. This discrepancy may point to a more fundamental distinction between single- and multiparticle systems. Perhaps the heterogeneity of single-particle basins is effectively smoothed out in multiparticle systems due to the presence of collective degrees of freedom that can be optimized. As a result, the basins of the latter might tessellate configuration space more efficiently than the former, thus suggesting a collective origin of the Edwards hypothesis. The precise origin of this difference remains, for now, an open question.

The basin volume distribution further provides insight into algorithmic outcomes. The basin volume of an algorithm indeed reweighs the contribution of an IS relative to the uniform distribution,

$$\langle\hat{\varphi}_{\rm IS}\rangle_{\rm alg}=\sum_{\rm IS}\frac{V_{\mathcal{B}_{\rm IS}^{\rm alg}}}{V_{\rm tot}}\hat{\varphi}_{\rm IS} \qquad [5]$$

Because the uniform measure ensures $\mathbb{E}_{\rm IS}[\hat{\varphi}]=1$, having $\langle\hat{\varphi}_{\rm IS}\rangle_{\rm alg}>1$ indicates a nonuniform weighting across basins.

Jamming Density Results. As expected for systems with complex landscapes (e.g. refs. 52–54 for mean-field systems and refs. 55–57 for multiparticle systems), different optimization algorithms reach ISs at different "depths" in the landscape. Although the maximal radius $r_{\rm IS}$ achieved when starting within the basin of attraction of a particular IS is geometrically fixed, the probability of ending in that basin is algorithm dependent, as in Eq. **5**. We here consider the performance of three different VA algorithms, i) VA-max, ii) VA-min, and iii) force-min, as well as the VA-like scheme, iv) CALiPPSO. For the RLG, Lerner et al.'s force-min (58) is a VA reluctant algorithm that does not follow VV edges, while CALiPPSO is a greedy but nonlocal scheme (*SI Appendix*). Fig. 5*A* compares $\langle\hat{\varphi}_{\rm IS}\rangle_{\rm alg}$ obtained by averaging over both trajectories and realizations of disorder, starting from an initial density $\hat{\varphi}_{\rm in}=0$. In all cases, the results are markedly larger than the uniform sampling bound, $\mathbb{E}[\hat{\varphi}_{\rm IS}]=1$, mentioned above. As expected, VA-max gives the lowest jamming densities in all d, thus identifying $\hat{\varphi}_{\rm J0}=\langle\hat{\varphi}_{\rm IS}\rangle_{\text{VA-max}}$ for $\hat{\varphi}_{\rm in}=0$; CALiPPSO gives nearly indistinguishable results. Remarkably, VA-min and force-min produce nearly identical results (albeit over a more limited d range), just as VA-max and CALiPPSO do. The gap between these two pairs of algorithms, however, grows with d, thus underscoring the growing complexity of the optimization landscape.

In order to relate these finite-d findings with the exact DMFT results for the limit $d\to\infty$—once they become available—a dimensional extrapolation is needed. A simple $1/d$ scaling, however, does not capture the trend of even the highest d results achieved, in marked contrast from what is observed for equilibrium observables in that same model (59). Recent results for other systems with complex landscapes suggest that an altogether different finite-size scaling form, d^{-a} with $a<1$, is to be expected (53, 60), but limited theoretical guidance is available for choosing a. Unfortunately, that choice substantially impacts the extrapolation outcome, with the systematic error far exceeding the statistical one. For instance, in the limit $d\to\infty$, $a=1/2$ gives $\hat{\varphi}_{\rm J0}=2.49(2)$ at one extreme, and $a=1/4$ gives $\hat{\varphi}_{\rm J0}=3.09(2)$ at the other (fits are for $d>30$). This density range is nevertheless largely consistent with earlier estimates obtained by GD on a softened RLG (31) and by force-min on the many-body problem (61) [after appropriate rescaling (31)], especially given that these estimates were obtained from narrower d ranges and extrapolated with $a=1$.

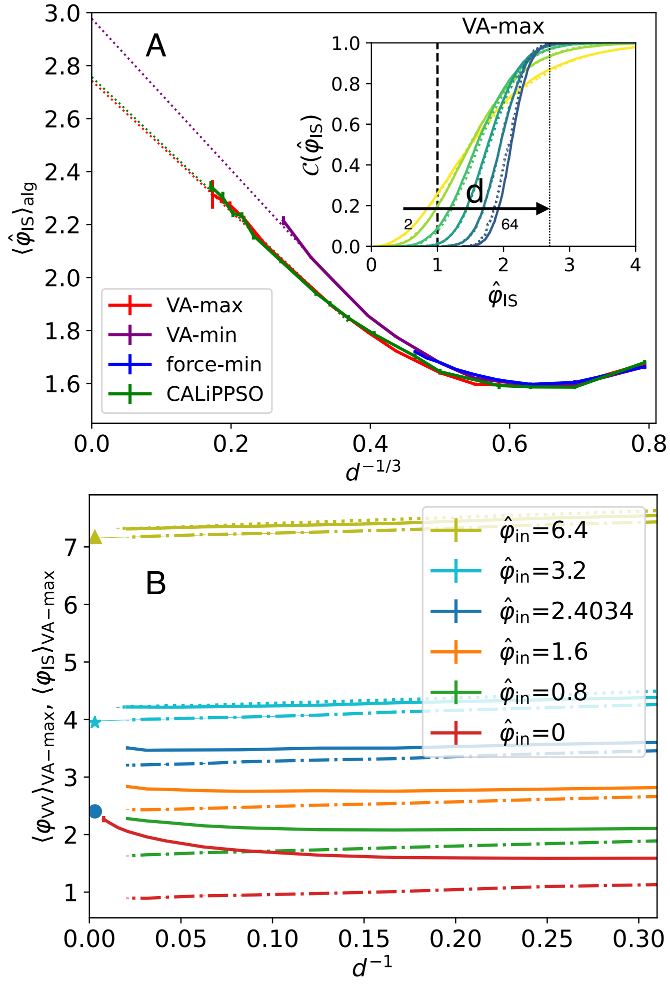

Fig. 5. (*A*): Dimensional dependence of the jamming density reached from $\hat{\varphi}_{\rm in}=0$, $\langle\hat{\varphi}_{\rm IS}\rangle_{\rm alg}$, for VA-max, VA-min, force-min, and CALiPPSO. The empirical scaling $d^{-1/3}$ gives a (nearly) linear scaling in large d. Both VA-max, the greediest local algorithm, and CALiPPSO, its nonlocal equivalent, achieve similar densities. Their extrapolation (thin dotted lines) suggests that $\hat{\varphi}_{\rm J0}=\langle\hat{\varphi}_{\rm IS}\rangle_{\text{VA-max}}=2.73(2)$ in the limit $d\to\infty$. For all $d>2$, VA-min and force-min give significantly denser results, with $\langle\hat{\varphi}_{\rm IS}\rangle_{\text{VA-min}}=2.94(9)$ asymptotically. *Inset*: The cumulative distribution of $\hat{\varphi}_{\rm IS}$ for VA-max (full lines) in $d=2\ldots64$ markedly sharpens as d increases. CALiPPSO results (dotted lines) are almost indistinguishable on this scale. The expected value for the uniform measure over ISs (dashed vertical line) as well as $\hat{\varphi}_{\rm J0}$ in the limit $d\to\infty$ (dotted vertical line) are given as reference. (*B*): Dimensional dependence of $\langle\hat{\varphi}_{\rm IS}\rangle_{\text{VA-max}}$ (full lines) and of the finite-d estimate of $\langle\hat{\varphi}_{\rm VV}\rangle_{\text{VA-max}}$ (dashed-dotted lines) reached from various $\hat{\varphi}_{\rm in}$. [The red curve is the same as in (*A*)]. For $\hat{\varphi}_{\rm in}\gg\hat{\varphi}_{\rm d}$, $\hat{\varphi}_{\rm G}$ (symbols) agrees with $\langle\hat{\varphi}_{\rm VV}\rangle_{\text{VA-max}}$ obtained by a linear extrapolation in $1/d$ (thin line), but not so for $\hat{\varphi}_{\rm in}\gtrsim\hat{\varphi}_{\rm d}$. Dotted lines indicate the VA-min curve for $\hat{\varphi}_{\rm in}=3.2$ and 6.4, closely matching the VA-max curve at these densities.

Gardner Transition. Trajectories can also be started from finite initial (equilibrium) densities, i.e., $\hat{\varphi}_{\rm in}>0$. Algorithms are then expected to reach ISs that lie deeper in the landscape, as shown for VA-max in Fig. 5*B*. Recall that in the limit $d\to\infty$, for $\hat{\varphi}_{\rm in}<\hat{\varphi}_{\rm d}=2.4034\ldots$ the equilibrium dynamics of the RLG is ergodic, while for $\hat{\varphi}_{\rm in}>\hat{\varphi}_{\rm d}$ it is localized to a cage (32). In the latter regime, a slow (adiabatic) compression as the tracer remains inside its cage makes state following calculations possible (see (10, Ch. 6) for details). For each $\hat{\varphi}_{\rm in}$, there then exists a corresponding Gardner packing fraction $\hat{\varphi}_{\rm G}(\hat{\varphi}_{\rm in})$, at which the cage fractures into a full hierarchy of subcages, a transition known as full replica symmetry breaking (fullRSB). Simulations further hint that a Gardner-like transition might be generally observable in a fast (nonadiabatic) compression, but theoretical guidance is lacking (17).

The simplicity of the RLG landscape geometry makes a broader consideration of Gardner physics possible. Recall that the initial VA projection collapses trajectories onto the first VV. In other words, a whole compact volume is reduced to a point. After this projection, the system explores the intricacies of the Voronoi edges that underlie landscape roughness (Fig. 4). The end of the projection phase at volume fraction $\hat{\varphi}_{\mathrm{VV}}$ therefore signals a dynamical transition analogous to the (adiabatic) Gardner transition in the limit $d \to \infty$, where the landscape becomes truly rough. Unlike the adiabatic transition, however, this dynamical transition can be observed for *all* $\hat{\varphi}_{\mathrm{in}}$.

Fig. 5*B* reports the dimensional evolution of $\hat{\varphi}_{\mathrm{dG}} = \langle \hat{\varphi}_{\mathrm{VV}} \rangle$, which in the limit $d \to \infty$ defines a dynamical Gardner transition. Unlike the jamming transition, $\hat{\varphi}_{\mathrm{dG}}$ clearly scales as $1/d$, consistent with its location being controlled by compact rather than rough landscape features. Its extrapolation to the limit $d \to \infty$ is therefore numerically robust. Interestingly, for $\hat{\varphi}_{\mathrm{in}} \gtrsim \hat{\varphi}_{\mathrm{d}}$ the adiabatic and the dynamical Gardner transitions are clearly distinct, with $\hat{\varphi}_{\mathrm{dG}} > \hat{\varphi}_{\mathrm{G}}$. For $\hat{\varphi}_{\mathrm{in}} \gg \hat{\varphi}_{\mathrm{d}}$, however, the two nearly coincide. In this regime, the tracer is caged within a nearly convex polytope, for which jamming is algorithm-independent. All algorithms—be they greedy or adiabatic—systematically converge to the center of the sphere inscribed in that polytope (33). In this limit, the Gardner dynamical transition can then be defined as the point at which the shrinking cage loses its first facet (i.e. at the first Voronoi vertex). At this point, compression begins to experience bifurcations, thus mirroring the $d \to \infty$ Gardner transition, at which point the replica symmetric (i.e., convex) solution becomes unstable and gives way to a multiplicity of solutions.

For $\hat{\varphi}_{\mathrm{in}} < \hat{\varphi}_{\mathrm{d}}$, no adiabatic transition exists, but the dynamical one smoothly continues across. The density gap between the jamming and the dynamical Gardner transitions further grows as $\hat{\varphi}_{\mathrm{in}}$ decreases and persists even at $\hat{\varphi}_{\mathrm{in}} = 0$. Finite-$d$ echoes of this physics should therefore be discernible along the compression trajectory of even the simplest of jamming systems, at least for $d > 2$.

Jamming Universality. Independent of the particular compression algorithm, isostatic jammed configurations have been reported to exhibit robustly universal properties. For many-body systems quantitative theoretical predictions obtained in the limit $d \to \infty$ (10) have indeed been found to persist down to $d = 2$ (16, 17). Given that these critical scalings only emerge in the thermodynamic limit, this collective effect would not be expected to hold as-is for the single-particle RLG. The distribution of gaps between nontouching obstacles, for instance, remains far from the $d \to \infty$ scaling with $\gamma = 0.4127\ldots$ even at the highest d reached (Fig. 6 *A*, *Inset*). The small force distribution, however, does exhibit a power-law regime compatible with the predicted exponent, $\theta = 0.4231\ldots$, even in fairly low d. This is confirmed by the finite-size scaling analysis of Fig. 6*A* for VA-max, using a squared-force normalization at each IS (see *SI Appendix* for details). The difference in d scaling between the two observables is consistent with their finite-size dependence in many-body systems (17). While the anomalous force distribution can be observed in fairly small systems, hints of the gap distribution require at least 200 particles.

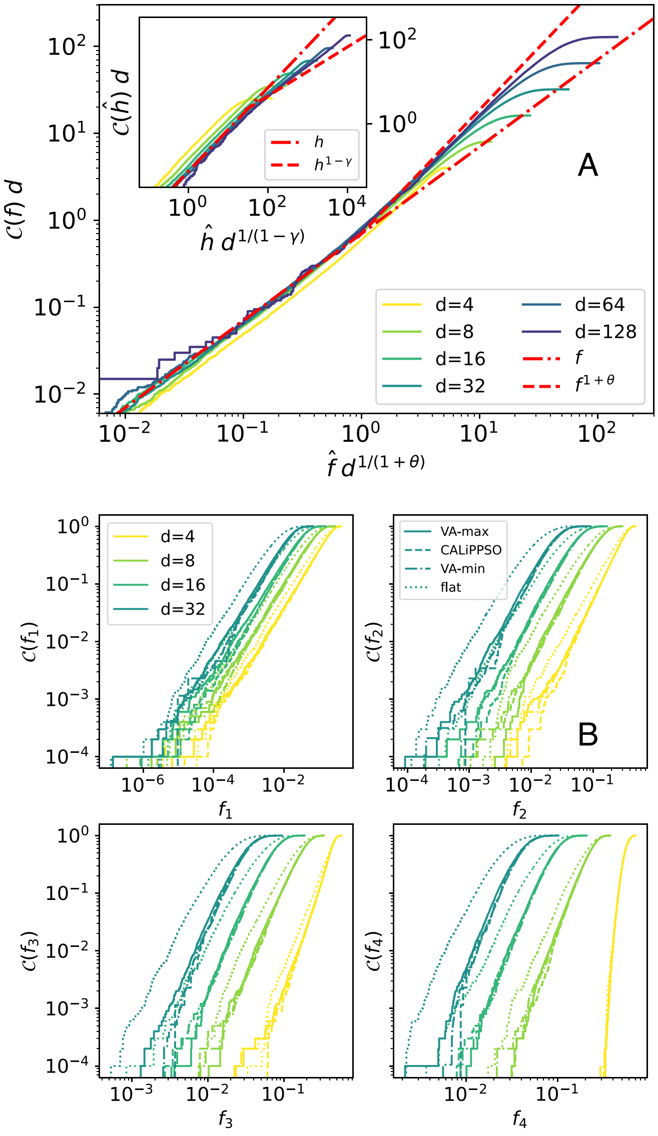

Fig. 6. (*A*): Scaled cumulative force distribution for the rescaled force $\hat{f} = f/\langle f \rangle$ for VA-max ISs reached from $\varphi_{\mathrm{in}} = 0$. The rescaling results in a very good collapse and a clear crossover from the linear regime (dash-dotted line) to the anomalous power-law regime (dashed line), $f^{1+\theta \ldots}$ with $\theta = 0.4231\ldots$. (*Inset*) The cumulative gap distribution does not similarly present an anomalous regime (with $\gamma = 0.4127\ldots$), consistent with the expected larger finite-d correction (see text). (*B*): Cumulative distribution of the smallest f_k contact force for $k = 1\ldots4$ for each IS in $d = 4, 8, 16, 32$. For each force type and each d, four different algorithms are considered: VA-max, CALiPPSO, VA-min, and uniform (flat) sampling. The resulting force distributions are identical for the first three, but differs for the uniform sampling. This supports the geometric universality observed in jamming physics.

More striking is that the geometry of isostatic contact vectors is robust even for small d. Different algorithms achieve IS with similarly distributed obstacles—an observation also made in multiparticle systems (25). As shown in Fig. 6*B*, for instance, the cumulative distribution of the k-smallest force, f_k, for $k = 1\ldots4$ changes with d but not with algorithm. VA-max, CALiPPSO, VA-min all give nearly indistinguishable results. Only the uniform sampling yields a distinct result. This difference can be interpreted—by analogy with potential energy landscape analysis—through the concepts of marginal and gapped IS. We conjecture that all sufficiently greedy (and sufficiently local) dynamics converge to marginal ISs and that all such marginal ISs belong to a common jamming universality class, but a geometric definition of marginality in nonsmooth energy landscapes is still lacking. We conclude that the structural universality of jamming is present in small d, encoded by the landscape and independent of the specific dynamics. The algorithm merely sets the overall scale. A purely geometric analysis of marginal ISs should therefore be able to extract the jamming critical exponents and hence fully explain their universality.

Conclusions. In this work, we have studied the landscape geometry and the volume ascent class of optimization algorithms for a paradigmatic model of real-space jamming, the random Lorentz gas. By analytically studying the complexity of its inherent structures, we have shown that in large dimensions, (phase) space is almost completely filled with volumes that are unstable under compression and we have identified the geometric origin of the ensuing landscape roughness. The basins of attraction therefore exhibit a growing hierarchical and fractal structure as d increases, a complexity reminiscent of what is reported for the many-body case (62). The greedy VA-max algorithm was further argued to be an optimal choice for computing φ_{J0}.

Through the landscape analysis, we have identified *en passant*, a dynamical analogue of a Gardner transition that should be experimentally accessible, and shown that static analytical predictions for $d \to \infty$ agree with this definition for VA algorithms. We have also found that the structure of jammed configurations is unaffected by the choice of jamming algorithm and converges to mean-field predictions in the limit $d \to \infty$, indicating a geometric origin for jamming universality.

Several research directions stem from these results. First, a generalization of VA-max to multiparticle systems should be possible. It would then be interesting to consider whether these systems exhibit similar landscape properties as their single-particle counterpart. Given the lower computational complexity of the algorithm compared to previous proposals, a thermodynamic estimate of φ_{J0}—a more physically and mathematically robust quantity than RCP—should then also be within reach. Second, solving the DMFT equations associated with the VA-max algorithm enables a direct investigation of the dynamics in the infinite-d limit and a more accurate extrapolation of the asymptotic packing fraction. This contrasts with previous methods (31), which required first extrapolating to infinite time at finite softness and then taking the zero-softness limit-an indirect and potentially less reliable procedure. An exact solution of the scheme in the limit $d \to \infty$ should therefore be within reach. Third, the algorithmic robustness of jamming could be used to derive scaling laws from a purely geometrical approach.

In addition, the present work sheds light on the broader class of real-space optimization problems in complex landscapes. "Computing largest empty circles with location constraints" (63), for instance, is a fundamental problem in robust optimization (38, 64, 65). Although heuristic algorithms can approximate its optimal solution in any dimension (66), the best optimizers are based on the Voronoi tessellation (63, 67, 68), which is computationally prohibitive in high dimensions, requiring $O(n^{\lceil d/2 \rceil})$ operations for n constraints. The VA-edge class provides a geometrically intuitive and computationally efficient approach to this problem. By analogy to simulated annealing, the reluctant VA-min algorithm can indeed find robust optimal configurations for a modest computational cost, $O(nd^3)$ (*SI Appendix*).

Materials and Methods

To study the basins of attraction of the RLG, we employ two main computational methods: 1) the geometric partition of phase space, and 2) the dynamical evolution of various optimization algorithms. Method 1) relies on Voronoi tessellations obtained from the qhull package (42); method 2) relies on event-driven de novo implementations [VA-edge (69)] or adaptations [force-min (58) and CALiPPSO (30)]. Both methods consider a set of M obstacles inside a ball of volume M (with density set to unity). We take M to scale either linearly or quadratically with d, depending on the simulation type. In all cases, results are checked to be M-independent. (See *SI Appendix* for details).

Data, Materials, and Software Availability. Data relevant to this work have been archived and can be accessed at the Duke Digital Repository https://doi.org/10.7924/r46119g71 (70).

ACKNOWLEDGMENTS. G.F. thanks Gilles Bonnet for suggesting the invariance leading to Eq. **2** and acknowledges partial support from a postdoctoral fellowship from the Duke Center on Computational Thinking. P.C. thanks the late Sayan Mukherjee for many stimulating discussions as well as the Chimera group of La Sapienza for their hospitality during part of this work. This work was supported in part by a grant from the Simons Foundation (Grant No. 454937 to P.C.) and by the Centro Nazionale di Ricerca in High Performance Computing, Big Data and Quantum Computing, Project CN_00000013, CUP B83C22002940006, National Recovery and Resilience Plan Mission 4 Component 2 Investment 1.4, Funded by the European Union–NextGenerationEU.

1. D. Frenkel, The tetrahedral dice are cast . . . and pack densely. *Physics* **3**, 3 (2010).
2. A. J. Liu, S. R. Nagel, Jamming is not just cool any more. *Nature* **396**, 21–22 (1998).
3. M. Manti, V. Cacucciolo, M. Cianchetti, Stiffening in soft robotics: A review of the state of the art. *IEEE Robot. Autom. Mag.* **23**, 93–106 (2016).
4. E. Lawson-Keister, M. L. Manning, Jamming and arrest of cell motion in biological tissues. *Curr. Opin. Cell Biol.* **72**, 146–155 (2021).
5. S. Spigler *et al.*, A jamming transition from under-to over-parametrization affects generalization in deep learning. *J. Phys. A* **52**, 474001 (2019).
6. S. d'Ascoli, M. Refinetti, G. Biroli, F. Krzakala, Double trouble in double descent: Bias and variance(s) in the lazy regime. *Proc. Mach. Learn. Res.* **119**, 2280–2290 (2020).
7. A. J. Liu, S. R. Nagel, The jamming transition and the marginally jammed solid. *Annu. Rev. Condens. Matter Phys.* **1**, 347–369 (2010).
8. L. Berthier, G. Biroli, Theoretical perspective on the glass transition and amorphous materials. *Rev. Mod. Phys.* **83**, 587 (2011).
9. S. Torquato, F. H. Stillinger, Jammed hard-particle packings: From Kepler to Bernal and beyond. *Rev. Mod. Phys.* **82**, 2633 (2010).
10. G. Parisi, P. Urbani, F. Zamponi, *Theory of Simple Glasses: Exact Solutions in Infinite Dimensions* (Cambridge University Press, 2020).
11. M. Wyart, Marginal stability constrains force and pair distributions at random close packing. *Phys. Rev. Lett.* **109**, 125502 (2012).
12. E. Lerner, G. Düring, M. Wyart, Low-energy non-linear excitations in sphere packings. *Soft Matter* **9**, 8252–8263 (2013).
13. M. Müller, M. Wyart, Marginal stability in structural, spin, and electron glasses. *Annu. Rev. Condens. Matter Phys.* **6**, 177–200 (2015).
14. A. Donev, S. Torquato, F. H. Stillinger, Pair correlation function characteristics of nearly jammed disordered and ordered hard-sphere packings. *Phys. Rev. E* **71**, 011105 (2005).
15. M. Skoge, A. Donev, F. H. Stillinger, S. Torquato, Packing hyperspheres in high-dimensional Euclidean spaces. *Phys. Rev. E* **74**, 041127 (2006).
16. P. Charbonneau, E. I. Corwin, G. Parisi, F. Zamponi, Jamming criticality revealed by removing localized buckling excitations. *Phys. Rev. Lett.* **114**, 125504 (2015).
17. P. Charbonneau *et al.*, Finite-size effects in the microscopic critical properties of jammed configurations: A comprehensive study of the effects of different types of disorder. *Phys. Rev. E* **104**, 014102 (2021).
18. V. Babu, S. Sastry, Criticality and marginal stability of the shear jamming transition of frictionless soft spheres. *Phys. Rev. E* **105**, L042901 (2022).
19. Y. Wang, J. Shang, Y. Jin, J. Zhang, Experimental observations of marginal criticality in granular materials. *Proc. Natl. Acad. Sci. U.S.A.* **119**, e2204879119 (2022).
20. S. Torquato, T. M. Truskett, P. G. Debenedetti, Is random close packing of spheres well defined? *Phys. Rev. Lett.* **84**, 2064–2067 (2000).
21. P. K. Morse *et al.*, "Amorphous packings of spheres" in *Packing Problems in Soft Matter Physics: Fundamentals and Applications*, H. K. Chan, Ed. (Royal Society of Chemistry, 2025), pp. 109–141.
22. M. Ozawa, T. Kuroiwa, A. Ikeda, K. Miyazaki, Jamming transition and inherent structures of hard spheres and disks. *Phys. Rev. Lett.* **109**, 205701 (2012).
23. S. Chiu, D. Stoyan, W. Kendall, J. Mecke, *Stochastic Geometry and Its Applications* (Wiley, 2013).
24. R. D. Kamien, A. J. Liu, Why is random close packing reproducible? *Phys. Rev. Lett.* **99**, 155501 (2007).
25. S. Wilken, R. E. Guerra, D. Levine, P. M. Chaikin, Random close packing as a dynamical phase transition. *Phys. Rev. Lett.* **127**, 038002 (2021).
26. V. Bolton-Lum, R. C. Dennis, P. Morse, E. Corwin, The ideal glass and the ideal disk packing in two dimensions. arXiv [Preprint] (2024). http://arxiv.org/abs/2404.07492 (Accessed 18 October 2025).
27. F. H. Stillinger, T. A. Weber, Inherent structure theory of liquids in the hard-sphere limit. *J. Chem. Phys.* **83**, 4767–4775 (1985).

28. S. Torquato, Y. Jiao, Robust algorithm to generate a diverse class of dense disordered and ordered sphere packings via linear programming. *Phys. Rev. E* **82**, 061302 (2010).
29. C. Artiaco, P. Baldan, G. Parisi, Exploratory study of the glassy landscape near jamming. *Phys. Rev. E* **101**, 052605 (2020).
30. C. Artiaco, R. Díaz Hernández Rojas, G. Parisi, F. Ricci-Tersenghi, Hard-sphere jamming through the lens of linear optimization. *Phys. Rev. E* **106**, 055310 (2022).
31. A. Manacorda, F. Zamponi, Gradient descent dynamics and the jamming transition in infinite dimensions. *J. Phys. A* **55**, 334001 (2022).
32. G. Biroli *et al*., Interplay between percolation and glassiness in the random Lorentz gas. *Phys. Rev. E* **103**, L030104 (2021).
33. G. Bonnet, P. Charbonneau, G. Folena, Glasslike caging with random planes. *Phys. Rev. E* **109**, 024125 (2024).
34. P. K. Morse, E. I. Corwin, Geometric signatures of jamming in the mechanical vacuum. *Phys. Rev. Lett.* **112**, 115701 (2014).
35. M. De Berg, *Computational Geometry: Algorithms and Applications* (Springer, 2000).
36. F. P. Preparata, M. I. Shamos, *Computational Geometry: An Introduction* (Springer, 2012).
37. C. D. Toth, J. O'Rourke, J. E. Goodman, *Handbook of Discrete and Computational Geometry* (CRC Press, 2017).
38. A. Ben-Tal, L. El Ghaoui, A. Nemirovski, *Robust Optimization* (Princeton University Press, 2009).
39. P. K. Morse, E. I. Corwin, Local stability of spheres via the convex hull and the radical Voronoi diagram. *Phys. Rev. E* **108**, 064901 (2023).
40. H. Edelsbrunner, A. Nikitenko, M. Reitzner, Expected sizes of Poisson-Delaunay mosaics and their discrete Morse functions. *Adv. Appl. Probab.* **49**, 745–767 (2017).
41. R. Schneider, W. Weil, *Stochastic and Integral Geometry, Probability and Its Applications* (Springer, 2008).
42. C. B. Barber, D. P. Dobkin, H. Huhdanpaa, The Quickhull algorithm for convex hulls. *ACM Trans. Math. Softw.* **22**, 469–483 (1996).
43. J. G. Wendel, A problem in geometric probability. *Math. Scand.* **11**, 109–112 (1962).
44. F. H. Clarke, *Optimization and Nonsmooth Analysis* (SIAM, 1990).
45. M. Gaudioso, G. Giallombardo, G. Miglionico, Essentials of numerical nonsmooth optimization. *4OR* **18**, 1–47 (2020).
46. G. Parisi, On the statistical properties of the large time zero temperature dynamics of the SK model. *Fractals* **11**, 161–171 (2003).
47. S. F. Edwards, R. B. S. Oakeshott, Theory of powders. *Phys. A* **157**, 1080–1090 (1989).
48. A. Baule, F. Morone, H. J. Herrmann, H. A. Makse, Edwards statistical mechanics for jammed granular matter. *Rev. Mod. Phys.* **90**, 015006 (2018).
49. N. Xu, D. Frenkel, A. J. Liu, Direct determination of the size of basins of attraction of jammed solids. *Phys. Rev. Lett.* **106**, 245502 (2011).
50. S. Martiniani, K. J. Schrenk, K. Ramola, B. Chakraborty, D. Frenkel, Numerical test of the Edwards conjecture shows that all packings are equally probable at jamming. *Nat. Phys.* **13**, 848–851 (2017).
51. S. Martiniani, M. Casiulis, When you can't count, sample! computable entropies beyond equilibrium from basin volumes *Pap. Phys.* **15**, 150001 (2023).
52. G. Folena, S. Franz, F. Ricci-Tersenghi, Rethinking mean-field glassy dynamics and its relation with the energy landscape: The surprising case of the spherical mixed *p*-spin model. *Phys. Rev. X* **10**, 031045 (2020).
53. G. Folena, S. Franz, F. Ricci-Tersenghi, Gradient descent dynamics in the mixed *p*-spin spherical model: Finite-size simulations and comparison with mean-field integration. *J. Stat. Mech.* **2021**, 033302 (2021).
54. G. Folena, F. Zamponi, On weak ergodicity breaking in mean-field spin glasses. *SciPost Phys.* **15**, 109 (2023).
55. S. Sastry, P. G. Debenedetti, F. H. Stillinger, Signatures of distinct dynamical regimes in the energy landscape of a glass-forming liquid. *Nature* **393**, 554–557 (1998).
56. Y. Nishikawa, M. Ozawa, A. Ikeda, P. Chaudhuri, L. Berthier, Relaxation dynamics in the energy landscape of glass-forming liquids. *Phys. Rev. X* **12**, 021001 (2022).
57. P. Suryadevara, M. Casiulis, S. Martiniani, Mirages in the energy landscape of soft sphere packings. arXiv [Preprint] (2024). https://arxiv.org/abs/2409.12113 (Accessed 16 October 2025).
58. E. Lerner, G. Düring, M. Wyart, Simulations of driven overdamped frictionless hard spheres. *Comput. Phys. Commun.* **184**, 628–637 (2013).
59. G. Biroli, P. Charbonneau, G. Folena, Y. Hu, F. Zamponi, Local dynamical heterogeneity in simple glass formers. *Phys. Rev. Lett.* **128**, 175501 (2022).
60. V. Erba, F. Behrens, F. Krzakala, L. Zdeborová, Quenches in the Sherrington-Kirkpatrick model. *J. Stat. Mech.* **2024**, 083302 (2024).
61. P. Charbonneau, P. K. Morse, Jamming, relaxation, and memory in a minimally structured glass former. *Phys. Rev. E* **108**, 054102 (2023).
62. S. S. Ashwin, J. Blawzdziewicz, C. S. O'Hern, M. D. Shattuck, Calculations of the structure of basin volumes for mechanically stable packings. *Phys. Rev. E* **85**, 061307 (2012).
63. G. T. Toussaint, Computing largest empty circles with location constraints. *Int. J. Comput. Inf. Sci.* **12**, 347–358 (1983).
64. D. Bertsimas, O. Nohadani, K. M. Teo, Robust optimization for unconstrained simulation-based problems. *Oper. Res.* **58**, 161–178 (2010).
65. D. Bertsimas, D. B. Brown, C. Caramanis, Theory and applications of robust optimization. *SIAM Rev.* **53**, 464–501 (2011).
66. M. Hughes, M. Goerigk, M. Wright, A largest empty hypersphere metaheuristic for robust optimisation with implementation uncertainty. *Comput. Oper. Res.* **103**, 64–80 (2019).
67. B. Chazelle, An optimal convex hull algorithm in any fixed dimension. *Discrete Comput. Geom.* **10**, 377–409 (1993).
68. A. Okabe, A. Suzuki, Locational optimization problems solved through Voronoi diagrams. *Eur. J. Oper. Res.* **98**, 445–456 (1997).
69. G. Folena, Volume ascent edge algorithm. [GitHub]. https://github.com/giampaolofolena/Volume_Ascent_Edge_Algorithm (2025). Accessed 16 October 2025.
70. G. Folena *et al*., Data and Jupyter notebook from: The geometry of jamming algorithms in the random Lorentz gas. Duke Research Data Repository. https://doi.org/10.7924/r46119g71. Accessed 18 October 2025.